Astron. Astrophys. 328, 493–498 (1997)

ASTRONOMY
AND
ASTROPHYSICS

Sub-arcsecond resolution 2D (x,y,λ) spectrography of the emission line region of NGC 5929 with TIGER*

P. Ferruit[1,2], **E. Pécontal**[1], **A.S. Wilson**[2,3], **and L. Binette**[4]

[1] CRAL - Observatoire de Lyon, 9 av. Charles André, F-69561 Saint-Genis-Laval Cedex, France
[2] Astronomy Department, University of Maryland, College Park, MD 20742, USA
[3] Space Telescope Science Institute, 3700 San Martin Drive, Baltimore, Maryland 21218, USA
[4] ESO, Casilla 19001, Santiago 19, Chile

Received 3 July 1997 / Accepted 22 July 1997

Abstract. We report observations of the Seyfert 2 galaxy NGC 5929 with the integral field spectrograph TIGER. These 2D spectrographic data, with sub-arcsecond spatial resolution, consist of 394 flux-calibrated spectra, covering the [N II], Hα and [S II] emission associated with the two radio-lobes. The two optical line emission components have been kinematically separated using Gaussian fitting of the spectra. From this decomposition, we have derived line intensities, ratios and velocities for each component. Although the line-of-sight velocities of the clouds are consistent with normal rotational motions, their high internal velocity dispersions and spatial association with the radio components clearly indicate an interaction between the radio ejecta and the ambient medium. We discuss four specific models describing this interaction but conclude that none of them is completely satisfactory.

Key words: galaxies: NGC 5929 – galaxies: Seyfert – galaxies: jets

1. Introduction

NGC 5929 is a Seyfert 2 galaxy (see Wilson & Keel, 1989, and references therein, WK89 hereafter), forming an interacting pair with its companion NGC 5930 (Arp 90, Lewis & Bowen, 1993). It hosts a linear radio source with two lobes straddling an unresolved nuclear component (Ulvestad & Wilson 1984; Whittle et al., 1986, W86 hereafter; WK89; Su et al., 1996, S96 hereafter). Early comparisons between radio and ground-based optical observations have shown that the morphology and the kinematics of the [O III]$\lambda\lambda$4959, 5007 emission line structure of this object are tightly correlated with those of the radio structure (W86, WK89). Two emission line components were detected, one blueshifted (north-east [NE] component) and the other redshifted (south-west [SW] component), each one being associated with a radio lobe.

This apparently clear association between optical and radio emission has made NGC 5929 one of the prototypical examples of interactions between radio ejecta and the ambient medium. Bow shock (Taylor et al., 1992, TDA92 hereafter) and expanding plasmon (Pedlar et al., 1985, PDU85 hereafter) models have been proposed to explain this correlation. However, the high angular resolution HST narrow-band images have shown that the situation is much more complicated than expected, largely due to the presence of dust lanes partially obscuring the NE line emitting regions (Bower et al., 1994, B94 hereafter). By comparing these images with radio maps at similar spatial resolutions, S96 have concluded that neither the bow shock (TDA92) nor expanding plasmon (PDU85) models are able to account for the [O III] emission line structure. More recently, jet/cloud (Steffen et al., 1996, hereafter SGRP96) and jet/homogeneous ISM (Steffen et al., 1997, hereafter SGWRP97) interaction models have been proposed to explain NGC 5929's optical and radio morphologies.

In the following, we first present our TIGER observations of NGC 5929 (Sect. 2 and 3) and their results (Sect. 4). Last (Sect. 5), we discuss the correlation between optical and radio emissions, especially in the light of the improved bow shock model of Ferruit et al. (1997, FBSP97 hereafter).

2. Observations and data reduction

This set of 2D spectrographic data was acquired in April 1992, using the integral field spectrograph TIGER mounted on the 3.60 m CFH Telescope. A detailed description of the instrument, which uses a micro-lenslet array, can be found in Bacon et al. (1995).

The two 1800 s spectrographic exposures of NGC 5929, centered east and west of the nucleus, are partially overlapping. With a total field of $10'' \times 6''$, they cover the whole emission

Send offprint requests to: P. Ferruit (pierre@astro.umd.edu)

* Based on observations collected at Canada-France-Hawaii Telescope, which is operated by CNRS of France, NRC of Canada, and the University of Hawaii

line region associated with the two radio lobes. The spatial sampling was 0.39″, with typical seeing conditions of 0.8″ FWHM. We covered a wavelength range of 500 Å centered on 6750 Å (including the [N II]λλ6548, 6583, Hα and [S II]λλ6716, 6731 lines) with a spectral sampling of 1.8 Å.

The data reduction has been performed using the specific TIGER software (Rousset 1992). Residuals from the wavelength calibration relation are smaller than 0.1 Å, much less than the 1.8 Å size of the spectral pixel. The spectral resolution is 3.6 Å FWHM, i.e. 160 km s^{-1} at 6750 Å. The heliocentric correction (-3.2 km s^{-1}) has been neglected.

The spectra were flux calibrated by means of observations of the standard star HZ 44 star. Comparison of the spectra of the two observed standard stars (Feige 34 and HZ 44) reveals differences of up to 15 % (non-photometric night). From our data, we derive a total Hα flux of 1.16 10^{-13} erg cm^{-2} s^{-1} within a 4.7″ diameter aperture, consistent to within 15 % of the 1.34 10^{-13} erg cm^{-2} s^{-1} flux found by Keel et al. (1985).

The two spectrographic exposures have been merged using the continuum center of the galaxy as a reference position. The achieved final 2D datacube consists of 394 flux calibrated spectra covering a 10″×6″ field with a 0.8″ spatial resolution.

Throughout this paper, we will use a heliocentric recession velocity of 2492±8 km s^{-1} for NGC 5929 (Nelson & Whittle, 1995). Using H_0=75 km s^{-1} Mpc^{-1}, this leads to a distance of 35.1 Mpc and a spatial scale of 170.3 pc arcsec^{-1}.

3. Analysis of spectral data

The stellar continuum has been fitted by a straight line over line free wavelength ranges and subtracted. No correction for any underlying Hα absorption has been attempted. To disentangle the two line emission components, we performed Gaussian fitting over the whole continuum subtracted data cube, using the FITSPEC software (Rousset 1992). We have assumed two emission-line velocity systems [1], one redshifted (SW component), and the other blueshifted (NE component). Although the profiles derived from models of the interaction between radio ejecta and the ambient medium interaction are non-Gaussian, no clear asymmetry has been found in our spectra, likely due to smoothing by our medium spectral resolution (see Fig. 3 and 4). Uncertainties in the fitted intensities have been derived using the rms of the fit's residuals.

4. Results

Table 1 displays the integrated spectral properties of the two emission line components, derived from Gaussian fits to the observed spectrum of NGC 5929.

In addition to the A to C line-emitting clouds defined by B94, we have labeled two other components (see Fig. 1): D, which corresponds to the eastern extended cloud seen in the HST [O III] image (B94); and E, which was seen in the [O III] image of W86 but too faint to be detected in the deconvolved pre-costar HST [O III] image (B94).

[1] Each system includes the [N II]λλ6548, 6583, Hα λ6563 and [S II]λλ6716, 6731 lines, sharing the same velocity and FWHM.

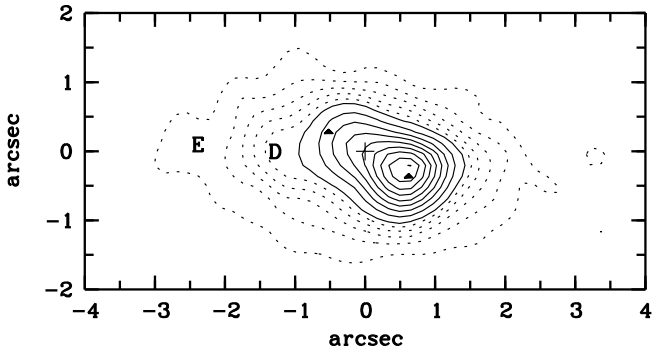

Fig. 1. Reconstructed [N II]λλ6548, 6583 + Hα image. The position of the nucleus is labeled by a cross, whereas those of the two radio lobes are marked by filled triangles. In addition, we have outlined the positions of two emission line regions (D and E). Units: 10^{-16} erg cm^{-2} s^{-1} arcsec^{-2}. Isophotes: 40 to 200 with an increment of 40 (dotted lines), 240 to 880 with an increment of 80 (solid lines). North is up, east is left.

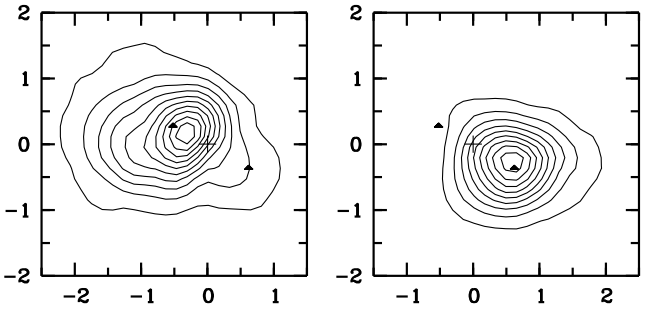

Fig. 2. Reconstructed Hα image of the NE (left) and SW (right) velocity components. The elongation toward the SW seen in the NE component map (left) is due to contamination by the SW component during the fitting process. The position of the nucleus is labeled by a cross, whereas those of the two radio lobes are marked by filled triangles. Units: 10^{-16} erg cm^{-2} s^{-1} arcsec^{-2}. Isophotes: 20 to 200 with an increment of 20 (left), 40 to 360 with an increment of 40 (right). North is up, east is left.

The individual Hα maps of the NE and SW velocity components are shown in Fig. 2. The NE, fainter, component, is spatially resolved with two main regions (the region of the weak E component is not plotted): the first is close to the nucleus and includes the B and C clouds and the diffuse [N II]-Hα emission observed by B94 in the vicinity of the nucleus; the second corresponds to component D. These two regions exhibit different spectral properties (Pécontal & Ferruit 1994). Their velocities and line ratios are given in Table 2, together with those of the E component. On the contrary, the SW lobe is spatially unresolved in our data. Its spectral characteristics are given in Table 1.

Table 1. Integrated properties of the NE and SW components. The FWHMs have been corrected for the 3.9 Å instrumental broadening. The densities have been derived from the [S II]λ6716/[S II]λ6731 line ratio, assuming T = 10^4 K.

	v – 2492 km s^{-1}	FWHM km s^{-1}	Hα erg s^{-1}	[N II]λ6583 erg s^{-1}	[S II]λ6716 erg s^{-1}	[S II]λ6731 erg s^{-1}	n cm^{-3}	[N II]/Hα[1]	[S II]/Hα[2]
NE	–145	180	1.95 10^{39}	1.14 10^{39}	0.74 10^{39}	0.57 10^{39}	130	0.6	0.7
SW	+115	220	2.48 10^{39}	1.75 10^{39}	1.00 10^{39}	0.94 10^{39}	450	0.7	0.8

[1] [N II]λ6583 / Hα [2] ([S II]λ6716 + [S II]λ6731) / Hα

Table 2. Spectral characteristics of the B+C, D and E components of the NE lobe. Velocities are given in km s^{-1}. [N II]$_2$ corresponds to [N II]λ6583, [S II]$_1$ to [S II]λ6716 and [S II]$_2$ to [S II]λ6731.

ID	v – 2492	[N II]$_2$/Hα	[S II]$_{1+2}$/Hα	[S II]$_1$/[S II]$_2$
B+C	–175	0.47±0.02	0.48±0.06	1.16±0.13
D	–175	0.84±0.06	0.9±0.2	1.03±0.15
E	–140	0.7±0.1	0.9±0.3	1.2±0.3

5. Discussion

5.1. The NE component

As outlined by S96, the relationship between radio and optical material in the NE component is unclear due to obscuration by a dust lane (B94). However, we point out that the two additional components to the NE – D and E – have no radio counterpart, while displaying projected negative velocities similar (component D) or only slightly lower (component E) than that of the B+C component (see Table 2). This shows that the radio material barely disturbs the line-of-sight velocities of the gas in clouds B and C, which are associated with the NE radio component.

Being unrelated to the radio material, the D and E components are likely to be photoionized by the AGN. In addition, they both display higher [N II]/Hα line ratios than the B+C component (see Table 2). In pure photoionization models, these changes in the [NII]/Hα line ratio could reflect changes in either the ionization parameter or the relative proportion of matter-bounded and ionization-bounded clouds (Binette et al. 1997), but no conclusion can be drawn from a single line ratio. Within our error bars, we do not detect any significant change in the [S II] density sensitive line ratio (see Table 2).

5.2. The relation between radio and optical emissions

The NE and SW clouds are aligned in PA $\simeq 60°$ which is quite close to the PA $\simeq 45°$ of the galaxy major axis (Schmitt et al., 1997). Comparison of the observed cloud recession velocities with the central stellar velocity dispersion (285 km s^{-1} FWHM, integrated over a $1.5'' \times 2.3''$ rectangular aperture positioned along PA=45°, Nelson & Whittle, 1995) and with the projected full rotation amplitude along the major-axis of the galaxy (290 km s^{-1}, Whittle, 1992) suggests that the observed cloud velocities (see Table 1 and 2) are largely consistent with normal rotational motions.

However, the nuclear FWHM of the [O III]λ 5007 line (415 km s^{-1}, Nelson & Whittle, 1995) is significantly higher than the FWHM of the stellar velocity dispersion. Also, our own measurements indicate an internal velocity spread of ≈ 200 km s^{-1}for each of the NE and SW clouds, suggesting that the AGN does affect the velocity dispersion of the ionized gas. In addition, the close association between the radio material and the [O III] clouds indicates that an interaction between the radio ejecta and the ambient gas is going on. These results lead us to investigate various models in which a radio plasmon or jet interacts with the ambient medium.

In the following, we focus on the SW component, less obscured than the NE one, and therefore more suited to study the relation between radio and optical emissions. Given the absence of perturbation of the observed radial velocities by the jet, it must lie close to the plane of the sky and possibly in the galactic plane, given the low inclination of the galaxy disk (26° inclination, 45° major-axis PA, Schmitt et al., 1997; 18° inclination, Whittle, 1992).

Therefore, we have chosen two illustrative values – 0° and 30° – for the angle between the jet and the plane of the sky and we will assume that the jet perturbs the line-of-sight velocity by at most only a few tens of km s^{-1} and the line widths by ≃100 - 200 km s^{-1}.

5.2.1. Expanding plasmon model

The expanding radio plasmon model (PDU85) does not easily account for the [O III] emission's morphology (B94). Indeed, it requires the shocked gas to be confined to a thin shell around the plasmon, whereas the [O III] emission is extended and located between the plasmon and the nucleus (B94; S96). In addition, using a plasmon radius of 5 pc (its size is 7 pc × 3 pc, S96) and a minimum internal energy in magnetic fields and relativistic particles of 1.9×10^{52} erg (S96), we derive an expansion velocity of $7800 \times (n_o/1\,\mathrm{cm}^{-3})^{-1/2}$ km s^{-1}(PDU85, equation 2; n_o is the density of the ambient medium) leading to an extremely hot shocked gas, unable to account for any optical forbidden line emission like [O III]λ 5007.

5.2.2. Jet/cloud interaction model

The jet/cloud interaction model (SGRP96) in which the head of the jet is followed by an expanding cocoon, explains well the

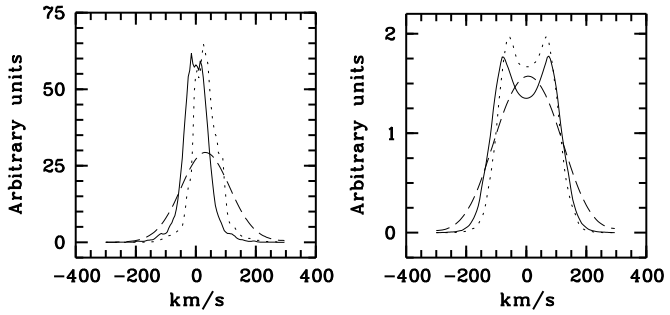

Fig. 3. Left panel: integrated Hα line profile for the jet/cloud interaction model (from SGRP96) for jet axis inclinations of 0° (solid line) and 30° (dotted line; the jet's component of motion along the line-of-sight is away from the observer). The last profile (dashed line) corresponds to the 30° one smoothed to a spectral resolution of 160 km s^{-1} similar to that of the TIGER data. See SGRP96 for a complete description of the model's parameters. Right panel: integrated Hα line profile for the jet/homogeneous ISM interaction (from SGWRP97) for jet axis inclinations of 0° (solid line) and 30° (dotted line; the jet's component of motion along the line-of-sight is away from the observer). The last profile (dashed line) corresponds to the 30° one smoothed to a spectral resolution of 160 km s^{-1}. See SGWRP97 for a complete description of the model's parameters.

fainter extended halo seen in the HST images. However, in this model, the main bulk of the emission comes from a very small shell (smaller than 10 pc, SGRP96) in front of the radio hot spot, whereas in NGC 5929, the SW emission peak is located behind the radio peak (S96) and has an extension of $\simeq$ 20 pc (B94).

For jet inclination angles of 0° to 30° relative to the plane of the sky, the Hα profiles (see Fig. 3, left panel) derived from this model are shifted by less than 30 km s^{-1}and have a typical FWHM of $\simeq$100 km s^{-1}. Both the velocity shift and dispersion fall within the expected range. No deeper comparison of the synthetic line profiles with the observed ones has been performed as, at our spectral resolution, all the shape details are smoothed out (see the smoothed Hα profile in Fig. 3, left panel).

5.2.3. Jet/homogeneous ISM interaction model

This second model (SGWRP97) describes the propagation of a fast jet (6800 km s^{-1}) in a homogeneous, fully ionized ISM. It displays the same bow shock + cocoon association than the jet/cloud interaction model, but the optical line emission comes almost exclusively from the expanding cylindrical shell of cool, high density gas surrounding the over-pressured cocoon of jet's material. This leads to the double peaked line profile shown in Fig. 3 (right panel).

The observed Hα line does not display this double peaked profile, but as outlined in Fig. 3 (right panel, see the predicted Hα profile smoothed to our spectral resolution), our spectral resolution is too low to separate the two peaks. The predicted velocity shift is very small (+6 km s^{-1}), consistent with the value of less than a few tens of km s^{-1} derived from the observations. The FWHM ($\simeq$200 km s^{-1}) is in excellent agreement with the observations.

The predicted Hα emission structure (SGWRP97) can account for the observed diffuse emission halo located behind the radio lobe. However, as in this model the emitting gas is distributed in a thin, roughly cylindrical, shell of $\simeq$ 40 pc diameter, the halo in the HST images (B94) should display two sharp and bright emission edges on both sides of the radio-jet. In addition the predicted Hα flux (5.8 10^{37} erg s^{-1}, SGWRP97) is much lower than the observed one (see Table 1). However, it is difficult to reach any conclusions concerning the validity of this model as we are considering only a single set of input parameters. It would be valuable to explore this model further in an attempt to optimise the parameters for NGC 5929.

5.2.4. Bowshock model

The bow shock model of FBSP97 describes the interaction between a jet without any developed cocoon and an homogeneous ISM. Ionization of gas by a nuclear source of uv photons is also included. To apply it to NGC 5929's case, we have first set its geometrical input parameters. D_z, which roughly corresponds to the 'plasmon' size (7 pc × 3 pc, S96), has been set to 5 pc. To reproduce the lateral (relative to the jet axis) extension of cloud A (B94), we have chosen to use the $Z \propto R^2$ bow shock profile (C=1, fastest available increase of R with Z, Z being the jet axis coordinate). In addition, as the longitudinal extent of the emission of cloud A in the HST image (B94) is roughly 0.6″ (i.e. $\simeq$100 pc), we have considered only the emission coming from the first 100 pc of the bow shock.

Except for the magnetic parameter, which has been arbitrarily set at $\mathscr{B}_o$=3 μG cm$^{3/2}$, the other input parameters have been determined by running a small grid of bow shock models and trying to match the observed line fluxes and ratios. The best constraints on the ISM hydrogen number density (n_o=5 cm^{-3}) and bow shock velocity (V_o=700 km s^{-1}) were provided by the total observed Hα flux and density sensitive [S II] ratio while the [N II]/ Hα ratio was used to constrain the ionization parameter ($\mathscr{U}_o$=0.01). Note that the bow shock velocity was only loosely constrained, since it has less influence than the ISM density on the fluxes of the observed lines (which are generated in the dense, photoionized cooled gas component).

Using this set of parameters, we have computed the expected fluxes, maps and line profiles. The predicted total Hα flux (5.3 10^{39} erg s^{-1}) as well as the [N II]/ Hα (0.64) and [S II]λ6716/ [S II]λ6731 (0.94) line ratios are consistent with the observations, whereas the predicted [S II]$\lambda\lambda$6716, 6731/ Hα line ratio (0.34) is too low (see Table 1).

We failed to reproduce the HST [O III] and Hα images, as in our synthetic maps the [O III] emission structure is double peaked (one peak on each side of the radio jet with a separation of $\simeq$35 pc, see Fig. 4) and both [O III] and Hα peaks are located more than 80 pc behind the radio peak (assumed to coincide with the apex of the bow shock, see Fig. 4).

The predicted Hα profile is very similar to that derived from the jet/homogeneous ISM interaction model and is double peaked. This feature disappears once the profile is smoothed to our spectral resolution (see Fig. 4, right panel) and therefore

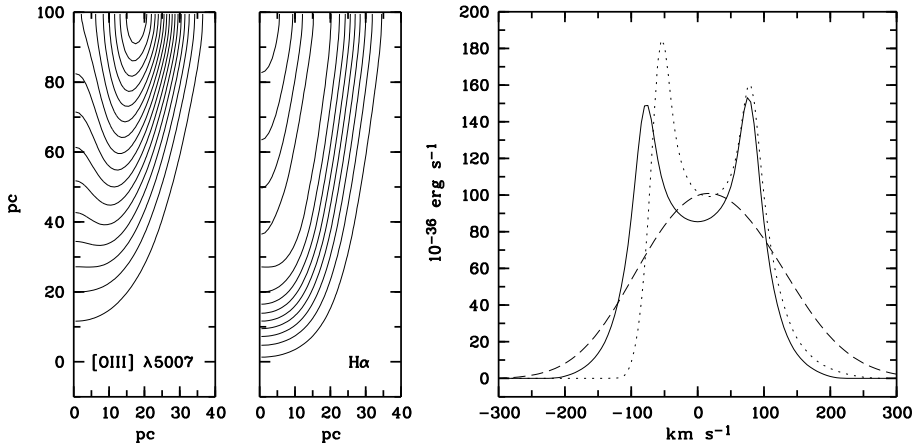

Fig. 4. Left panel: [O III] and Hα maps of the bow shock model smoothed to a 0.1″ spatial resolution for 0°inclination (i.e. the axis of the bow shock is in the plane of the sky). Only the right half of the maps are plotted as the model is symmetric relative to the y-axis; the direction of motion of the shock in this diagram is downwards. The origin corresponds to the apex of the bow shock. Isophotes : 0.1 to 1.6 with an increment of 0.1 ([O III]), 0.4 to 3.8 with an increment of 0.4 (Hα). Units: arbitrary. Right panel: integrated Hα line profile for bow shock inclinations of 0° (solid line) and 30° (dotted line; the bow shock's component of motion along the line of sight is away from the observer). The last profile (dashed line) corresponds to the 30° one smoothed to a spectral resolution of 160 km s^{-1} similar to that of the TIGER data.

cannot be used to rule out the bow shock model. As for the previous model, the velocity shift of the line profile ($\simeq$20 km s^{-1} for a 30° inclination) falls within the expected range, while the predicted FWHM of $\simeq$200 km s^{-1}is also consistent with the data.

5.3. Constraints on the ram pressure

In the expanding plasmon model (PDU85), the minimum internal energy in magnetic field and relativistic particles (U_{me}=1.9 10^{52} erg, S96) and the corresponding pressure (P_{me}=1.06 10^{-6} dyne cm^{-2}, S96) were used to derive the plasmon's expansion velocity (see Sect. 5.2.1) which has been found to be very high, leading us to rule out this model. In the same way and for the three other models, we can use the fact that P_{me} cannot be greatly in excess of the ram pressure to put constraints on the combination of the jet velocity and the density of the ambient medium.

In the jet/cloud interaction model of SGRP96, the velocity of the shock propagating in the cloud is $v_{shock} \simeq 200$ km s^{-1} for a cloud density of n_{cloud}=180 cm^{-3}, leading to a ram pressure which is almost one order of magnitude too low ($\simeq$ 2 10^{-7} (n_{cloud}/180 cm^{-3}) $\times$ (v_{shock}/200 km s^{-1})^2 dyne cm^{-2}). The best way to get values consistent with the observed P_{me} is likely to increase the shock velocity and/or the cloud density. Note, that this will lead to a Hα flux higher than the 6.3 10^{38} erg s^{-1} one derived for the current set of model parameters (SGRP96), which will therefore be closer to the observed value for cloud A (2.48 10^{39} erg s^{-1}, see Table 1).

For the jet/ISM model and for the set of parameters used in SGWRP97, the maximum predicted ram pressure (4 10^{-8} dyne cm^{-2}, SGWRP97, see their Fig. 1) is also much lower than the observed values. As for the jet/cloud interaction model, this problem is likely to be solved by increasing either the shock velocity or the ISM density.

Last, in the case of the bow shock model, and from Sect. 5.2.4, we derive a shock velocity of 700 km s^{-1} and an ISM density of 5 cm^{-3} in order to match the predicted optical line fluxes and ratios with the observed ones. This leads to a maximum ram pressure (at the apex of the bow shock) of 5 10$^{-8}\times$ (n_{ISM}/5 cm^{-3}) $\times$ (v_{shock}/700 km s^{-1})^2 dyne cm^{-2}, much lower than the value inferred from the relativistic pressure (1.06 10^{-6} dyne cm^{-2}). As the ISM density cannot be increased significantly without getting line fluxes and a density sensitive [S II] ratio inconsistent with the observations, we need to increase the shock velocity to 3000 km s^{-1} to obtain ram pressures in the 10^{-6} dyne cm^{-2} range. For such a high shock velocity, the gas entering the bow shock does not cool until $\simeq$100 pc from the apex, preventing low excitation forbidden lines like [N II] or [S II] from being emitted closer to the radio 'plasmon', contrary to observations. This is, therefore, a significant problem with this model.

6. Conclusion

From this 2D TIGER data cube, we have disentangled the two nuclear emission line components of NGC 5929. In the NE one, which is spatially resolved, the D and E clouds' recessional velocities are similar to those of the B+C region, despite the former clouds being unrelated to the radio ejecta. This stresses that the impact of the radio material on the line-of-sight velocities of the ambient gas is only marginal. However, the broadening of the lines and the close association with the radio clouds clearly indicate an interaction between the radio ejecta and interstellar gas. The D and E clouds also display a higher [N II]/Hα ratio than the B+C component. Our ground-based spatial resolution has prevented us from spatially resolving the SW emission-line component, so only integrated spectral properties have been derived for this cloud.

We have briefly discussed the properties of the SW cloud in the light of four published models of the interaction between ra-

dio ejecta and an ambient medium. In their present forms, none of the models provides a ram pressure comparable with the relativistic pressure inferred from the radio observations while at the same time accounting for the emission-line properties. The line of sight velocity and velocity dispersion in the SW cloud are well accounted for by the bow shock (FBSP97), jet/cloud (SGRP96) and jet/homogeneous ISM interaction (SGWRP97) models. All models predict edge-brightened bow shock or cylindrical shell structures for the ionized gas, which seems to conflict with the HST imaging.

High spatial resolution spectrography (e.g. with STIS) of NGC 5929 is needed to obtain the velocity structure of both the NE and SW components and to understand the relationship between the relativistic and thermal gases. Models of jet-ambient medium interactions with more extensive coverage of parameter space are also desirable.

Acknowledgements. We thank G. Bower for sending us his HST images, D.J. Saika for the 2 cm radio map and W. Steffen for providing us with the Hα line profiles derived from his models. This research has made use of the ADS abstract service.

References

Bacon, R., et al., 1995, A&A Supp., 113, 347
Binette, L., Wilson, A.S., Raga, A., and Storchi-Bergmann, T., 1997, A&A submitted
Bower, G.A., et al., 1994, AJ, 107, 1686
Ferruit, P., and Binette, L., 1996, Jet-Cloud Interactions in Active Galaxies, ed. N. Clark, Univ. of Sheffield, on-line proceedings
(http://www.shef.ac.uk/∼phys/research/astro/conf/index.html)
Ferruit, P., Binette, L., Sutherland, R.S., and Pécontal, E., 1997, A&A, in press
Keel, W.C., Kennicutt, R.C., Hummel, E., and van der Hulst, J.M., 1985, AJ, 90, 708
Lewis, J.R., and Bowen, D.V., 1993, MNRAS, 264, 818
Nelson, C.H., and Whittle, M., 1995, ApJ Supp., 99, 67
Pécontal, E., and Ferruit, P., 1994, IAU Symposium 159 - Multiwavelength continuum emission of AGN, ed T.J.-L. Courvoisier and A. Blécha, 445
Pedlar, A., Dyson, J.E., and Unger, S.W., 1985, MNRAS, 214, 463
Rousset A., 1992, Contribution des méthodes numériques au dépouillement des données du spectrographe intégral de champ TIGER, PhD Thesis, Univ. J.Monnet de Saint-Etienne.
Schmitt, H.R., Kinney, A.L., Storchi-Bergmann, T., and Antonucci, R., 1997, ApJ, 477, 623
Steffen, W., Gòmez, J.L., Williams, R.J.R., Raga, A.C., and Pedlar, A., 1997, MNRAS, 286, 1032
Steffen, W., Gòmez, J.L., Raga, A.C., and Pedlar, A., 1996, Jet-Cloud Interactions in Active Galaxies, ed. N. Clark, Univ. of Sheffield, on-line proceedings
(http://www.shef.ac.uk/∼phys/research/astro/conf/index.html)
Su, B.M., et al., 1996, MNRAS, 279, 1111
Taylor, D., Dyson, J.E., and Axon, D.J., 1992, MNRAS, 255, 351
Ulvestad, J. S. & Wilson, A. S. 1984, ApJ, 285, 439
Whittle, M., 1992, ApJS, 79, 49
Whittle, M., et al., 1986, MNRAS, 222, 189
Wilson, A.S., and Keel, W.C., 1989, AJ, 98, 1581

This article was processed by the author using Springer-Verlag LaTeX A&A style file *L-AA* version 3.